

Simulations and experiments of aperiodic and multiplexed gratings in volume holographic imaging systems

Yuan Luo,¹ Jose Castro,² Jennifer K. Barton,^{3,4} Raymond K. Kostuk,^{2,4} and George Barbastathis^{1,5}

¹Department of Mechanical Engineering, Massachusetts Institute of Technology, Cambridge 02139, Massachusetts, USA.

²Department of Electrical and Computing Engineering, University of Arizona, Tucson 85721, Arizona, USA

³Division of Biomedical Engineering, University of Arizona, Tucson, Arizona, USA.

⁴College of Optical Sciences, University of Arizona, Tucson, Arizona, USA.

⁵Singapore-MIT Alliance for Research and Technology (SMART) Centre, Massachusetts Institute of Technology, S16-06-17, 3 Science Drive 2, Singapore 117543

*yuan_luo@mit.edu

Abstract: A new methodology describing the effects of aperiodic and multiplexed gratings in volume holographic imaging systems (VHIS) is presented. The aperiodic gratings are treated as an ensemble of localized planar gratings using coupled wave methods in conjunction with sequential and non-sequential ray-tracing techniques to accurately predict volumetric diffraction effects in VHIS. Our approach can be applied to aperiodic, multiplexed gratings and used to theoretically predict the performance of multiplexed volume holographic gratings within a volume hologram for VHIS. We present simulation and experimental results for the aperiodic and multiplexed imaging gratings formed in PQ-PMMA at 488nm and probed with a spherical wave at 633nm. Simulation results based on our approach that can be easily implemented in ray-tracing packages such as Zemax[®] are confirmed with experiments and show proof of consistency and usefulness of the proposed models.

©2010 Optical Society of America

OCIS codes: (090.4220) Multiplexed hologram; (090.7330) Volume hologram; (110.0110) Imaging systems; (090.2890) Holographic optical elements.

References and links

1. W. Liu, D. Psaltis, and G. Barbastathis, "Real-time spectral imaging in three spatial dimensions," *Opt. Lett.* **27**(10), 854–856 (2002).
2. P. J. Gelsinger-Austin, Y. Luo, J. M. Watson, R. K. Kostuk, G. Barbastathis, J. K. Barton, and J. M. Castro, "Optical design for a spatial-spectral volume holographic imaging system," *Opt. Eng.* **49**(4), 043001–043005 (2010).
3. Y. Luo, S. B. Oh, and G. Barbastathis, "Wavelength-coded multifocal microscopy," *Opt. Lett.* **35**(5), 781–783 (2010).
4. Z. Li, D. Psaltis, W. Liu, W. R. Johnson, and G. Bearman, "Volume holographic spectral imaging," *Proc. SPIE* **5694**, 33–40 (2005).
5. A. V. Veniaminov, V. G. Goncharov, and A. P. Popov, "Hologram amplification by diffusion destruction of out-of phase periodic structures," *Opt. Spectrosc.* **70**(4), 505–508 (1991).
6. Y. Luo, P. J. Gelsinger-Austin, J. M. Watson, G. Barbastathis, J. K. Barton, and R. K. Kostuk, "Laser-induced fluorescence imaging of subsurface tissue structures with a volume holographic spatial-spectral imaging system," *Opt. Lett.* **33**(18), 2098–2100 (2008).
7. A. Sinha, and G. Barbastathis, "Volume holographic imaging for surface metrology at long working distances," *Opt. Express* **11**(24), 3202–3209 (2003).
8. H. Kogelnik, "Coupled wave theory for thick hologram grating," *Bell Syst. Tech. J.* **48**, 2909–2946 (1969).
9. G. Moharam, and T. K. Gaylord, "Three-dimensional vector coupled-wave analysis of planar-grating diffraction," *J. Opt. Soc. Am.* **73**(9), 1105–1112 (1983).
10. P. Wissmann, S. B. Oh, and G. Barbastathis, "Simulation and optimization of volume holographic imaging systems in Zemax," *Opt. Express* **16**(10), 7516–7524 (2008).
11. R. R. A. Syms, and L. Solyman, "Localized one-dimensional theory for volume holograms," *Opt. Quantum Electron.* **13**(5), 415–419 (1981).

12. R. R. A. Syms, and L. Solymar, "Analysis of volume holographic cylindrical lenses," *J. Opt. Soc. Am.* **72**(2), 179–186 (1982).
13. A. Sinha, and G. Barbastathis, "Broadband volume holographic imaging," *Appl. Opt.* **43**(27), 5214–5221 (2004).
14. A. Sinha, W. Sun, T. Shih, and G. Barbastathis, "Volume holographic imaging in transmission geometry," *Appl. Opt.* **43**(7), 1533–1551 (2004).
15. G. Barbastathis, and D. Psaltis, "Volume holographic multiplexing methods," in *Holographic Data Storage* (Springer, 2000).
16. Y. Luo, P. J. Gelsinger, J. K. Barton, G. Barbastathis, and R. K. Kostuk, "Optimization of multiplexed holographic gratings in PQ-PMMA for spectral-spatial imaging filters," *Opt. Lett.* **33**(6), 566–568 (2008).
17. R. K. Kostuk, Multiple grating reflection volume holograms with application to optical interconnects, Ph. D. Thesis at Stanford University, 1986.
18. Y. Luo, J. M. Russo, R. K. Kostuk, and G. Barbastathis, "Silicon oxide nanoparticles doped PQ-PMMA for volume holographic imaging filters," *Opt. Lett.* **35**(8), 1269–1271 (2010).
19. G. Barbastathis, and D. Psaltis, "Shift-multiplexed holographic memory using the two-lambda method," *Opt. Lett.* **21**(6), 432–434 (1996).
20. W. K. Maeda, "Edge-illumination gratings in PQ-doped PMMA for OCDMA applications," The University of Arizona, ECE Department, Thesis, 2005.
21. J. M. Russo, "Temperature dependence of holographic filters in phenanthrenequinone-doped poly(methyl methacrylate)," The University of Arizona, ECE Department, Thesis, 2007.
22. J. Rosen, and G. Brooker, "Non-scanning motionless fluorescence three-dimensional holographic microscopy," *Nat. Photonics* **2**(3), 190–195 (2008).

1. Introduction

Volume holographic imaging systems (VHIS) consisting of volume holographic gratings as specialized spatial-spectral filters have recently been successfully applied to microscopic and spectroscopic application. These include depth selective [1–3], hyper-spectral [4,5], and fluorescence imaging [6], and long working distance profilometry [7]. Therefore, an accurate methodology to predict the performance of volume holographic gratings is necessary to optimize their design and fabrication with different construction parameters.

Kogelnik's two-beam approximate coupled-wave (ACW) analysis [8] and rigorous coupled-wave (RCW) theory [9] have been used extensively to model diffraction effects of uniform gratings formed by two plane waves. Wissman [10] recently demonstrated to the analysis of planar holographic gratings with a k-sphere formulation to predict volumetric gratings' diffraction efficiency. However, the formation of aperiodic gratings with varied k-vectors is a process more complicated than that of the planar ones. Several attempts have been made to analytically evaluate varied k-vector holographic gratings. Syms and Solymar [11,12] demonstrated treating a grating with localized planar grating sections of variable in orientation across the hologram. However, it is based on wave optics and not convenient for design process. In Ref [13–15], the Born approximation was used to obtain analytical models for volume holographic gratings. This technique is based on wave optics under assumptions of weak interaction among the incident and diffracted light [8]. In case of volume holograms of high-diffractive efficiency, the approximation breaks down because the incident light is strongly depleted.

In this paper, we present a comprehensive methodology to model volumetric diffraction effects including depth selectivity and diffraction efficiency of curved gratings in volume holographic imaging systems (VHIS). In our method, aperiodic and multiplexed gratings will be analyzed by considering locally planar gratings based on Syms' method incorporating ray-tracing and coupled wave (ACW and RCW) theory. RCW with sequential ray-tracing and ACW analysis with non-sequential ray-tracing algorithms will be introduced. The coupled wave approach considers arbitrary polarization of the different fields in the diffraction process with any hologram thickness. With ray-tracing implementation, our approach can provide a fast estimation for characterizing volume holographic gratings in imaging systems. In addition, our approach can be extended to multiplexed gratings. The simulation results are compared and are found to agree well with experimental measurements of multiplexed volume holographic gratings formed in PQ-PMMA [16].

In Section 2, we review the relevant features of approximate and rigorous coupled wave theories used in our model. In addition, we describe the simulation procedure for aperiodic and multiplexed holographic gratings. In Section 3, experimental results using two

multiplexed volume holographic gratings in VHIS are measured to characterize volumetric diffraction effects. In Section 4, we investigate the consistency and accuracy of the proposed methodology and compare the simulation results with experimental measurements. Section 5 discusses advantages and limitations of our approach.

2. Model

2.1 Rigorous Coupled Wave Analysis

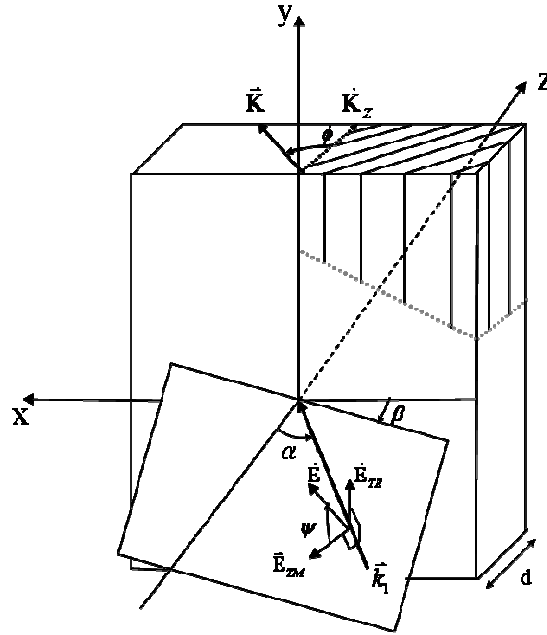


Fig. 1. Reconstruction geometry of a single slanted planar grating with a planar wave of propagation vector \vec{k}_i incident with an arbitrary angle and polarization.

RCW analysis [9] has been known to accurately predict the performance of a planar grating. The three-dimensional reconstruction geometry for a slanted planar grating is shown in Fig. 1. RCW analysis can compute the diffraction efficiency for any incident beam angle with arbitrary linear polarization state. It can model conical diffraction with grating vector, \vec{K} , lying outside the reconstruction plan, and it can also account for an arbitrary number of transmission and reflection orders for a hologram with thickness of d . In Fig. 1, a polarized electromagnetic wave is incident at an angle α . The polarization of the incident beam is given by ψ , which is the angle of the \vec{E} field vector with respect to the TM component. The plane of incidence has an angle β with respect to the x axis.

If we assume that the grating vector is in the x-z plane, the grating vector is given by:

$$\vec{K} = (K \sin \varphi) \hat{x} + (K \cos \varphi) \hat{z}, \quad (1)$$

where $K = 2\pi/\Lambda$, Λ is the grating period, and φ is the slant angle. The incident medium is region 1, region 2 is the grating recording medium, and region 3 is the substrate. The amplitude of the propagation vector in the ℓ th region k_ℓ is equal to $k\sqrt{\varepsilon_\ell}$, where ε_ℓ is the relative permittivity in region ℓ , $k = 2\pi/\lambda$, and λ is the free-space wavelength. In the incident medium, the incident normalized electric-field vector is

$$\vec{E}_{inc} = \hat{u} \exp(-j\vec{k}_1 \cdot \vec{r}), \quad (2)$$

where $\vec{k}_1 = k_1(\sin \alpha \cos \beta)\hat{x} + k_1(\sin \alpha \sin \beta)\hat{y} + k_1(\cos \alpha)\hat{z}$, $\vec{r} = x\hat{x} + y\hat{y} + z\hat{z}$, and \hat{u} is the polarization unit vector given by:

$$\begin{aligned} \hat{u} = & (\cos \psi \cos \alpha \cos \beta - \sin \psi \sin \beta)\hat{x} + \\ & (\cos \psi \cos \alpha \sin \beta + \sin \psi \cos \beta)\hat{y} - (\cos \psi \sin \alpha)\hat{z}. \end{aligned} \quad (3)$$

The normalized total electric fields in regions 1 and 3 are given by:

$$\vec{E}_1 = \vec{E}_{inc} + \sum_n \vec{R}_n \exp(-j\vec{k}_{1n} \cdot \vec{r}), \quad (4)$$

$$\vec{E}_3 = \sum_n \vec{T}_n \exp(-j\vec{k}_{3n} \cdot (\vec{r} - d\hat{z})), \quad (5)$$

where \vec{R}_n is the normalized vector electric field of the n th reflected wave in region 1 with propagation vector \vec{k}_{1n} , and \vec{T}_n is the normalized vector electric field of the n th transmitted wave in region 3 with propagation vector \vec{k}_{3n} . According to the phase matching condition, \vec{k}_{tn} in region 1 and 3 can be expressed as:

$$\begin{aligned} \vec{k}_{tn} = & k_{xn}\hat{x} + k_{yn}\hat{y} + k_{ztn}\hat{z} \\ = & [(\vec{k}_1 - n\vec{K}) \cdot \hat{x}]\hat{x} + [(\vec{k}_1 - n\vec{K}) \cdot \hat{y}]\hat{y} + k_{ztn}\hat{z}, \end{aligned} \quad (6)$$

where $k_{xn} = k_1 \sin \alpha \cos \beta - nK \sin \varphi$, $k_{yn} = k_1 \sin \alpha \sin \beta$, and $k_{ztn} = \sqrt{k_t^2 - k_{xn}^2 - k_{yn}^2}$. The sign of the propagation vector in the z direction, k_{z1n} and k_{z3n} , must be chosen carefully. k_{z1n} is negative real for a reflected propagating wave and positive imaginary for an evanescent wave. However, k_{z3n} is positive real for a transmitted propagating wave and negative imaginary for an evanescent wave.

The electric and magnetic fields in the region occupied by recording medium can be expressed as:

$$\vec{E}_2 = \sum_n [S_{xn}(z)\hat{x} + S_{yn}(z)\hat{y} + S_{zn}(z)\hat{z}] \exp(-j\vec{\sigma}_n \cdot \vec{r}), \quad (7)$$

$$\vec{H}_2 = (\varepsilon_0/\mu_0) \sum_n [U_{xn}(z)\hat{x} + U_{yn}(z)\hat{y} + U_{zn}(z)\hat{z}] \exp(-j\vec{\sigma}_n \cdot \vec{r}), \quad (8)$$

where ε_0 is the permittivity of free space, μ_0 is the permeability of free space, and $\vec{\sigma}_n = k_{xn}\hat{x} + k_{yn}\hat{y} - nK_z\hat{z}$. S_n and U_n are the amplitudes of the n th space-harmonic of the electric and magnetic fields so that \vec{E}_2 and \vec{H}_2 satisfy Maxwell's equations in the region 2:

$$\nabla \times \vec{E}_2 = -j\omega\mu_0, \quad (9)$$

$$\nabla \times \vec{H}_2 = j\omega\varepsilon_0\varepsilon(x, y, z)\vec{E}_2, \quad (10)$$

with ω the angular frequency of the incident radiation. $\varepsilon(x, y, z)$ is the periodic complex relative permittivity in the grating region (region 2). The method of solving S_n and U_n is to substitute Eq. (7) and (8) into (9) and (10). The detail of the process is described in Ref [9]. Once the general solution is obtained using numerical methods, the amplitudes of diffracted fields are calculated by matching the boundary conditions at each boundary of region 2. Then, the efficiency can be calculated for each diffracted order.

2.2 Approximate Coupled Wave Theory

Even though it is the most accurate, RCW analysis requires intensive computation, and it is difficult to utilize with iterative design algorithms. In the case of strong volume holograms, where one diffracted order is dominant in most cases, approximate couple wave (ACW) analysis [8] results in an analytical solution that is relatively accurate and easier to implement in optimization procedures. Therefore, ACW analysis can be easily implemented in ray-tracing packages such as Zemax[®]. Moreover, the analytical expressions of ACW provide useful insight of the VHIS operation which is helpful in the design process.

ACW analysis assumes that only two significant coherent light waves interact in the hologram grating during the diffraction process. In the case where $\beta = 0$, the replay beam is TE polarized, and the total electrical field for the beam in the grating in region 2 can be expressed as:

$$E_2 = S_0(z) \exp(-j\bar{k}_1 \cdot \hat{r}) + S_1(z) \exp(-j\bar{k}_d \cdot \hat{r}), \quad (11)$$

where \bar{k}_d represents the propagation vector of the diffracted wave. The diffraction efficiency (η) for a transmission holographic grating with the first order propagation in the positive direction in region 3 is given by

$$\eta = (|c_s| / c_R) S_1 S_1^*, \quad (12)$$

$$S_1 = -j(c_R / c_S)^{1/2} \exp(-\rho d / c_R) \exp(\xi) \frac{\sin(v^2 - \xi^2)}{(1 - v^2 / \xi^2)^{1/2}}, \quad (13)$$

$$v = \frac{\pi \cdot \Delta n \cdot d}{\lambda \sqrt{c_R c_S}}, \text{ and } \xi = \frac{d}{2} \left(\frac{\rho}{c_R} - \frac{\rho}{c_S} - j \frac{\mathcal{G}}{c_S} \right), \quad (14)$$

where Δn is index modulation of the hologram, ρ is absorption coefficient, $c_R = \cos(\alpha)$, $c_S = \cos(\alpha) - K_z / k_1$, and \mathcal{G} is the detuning parameter [8,17].

2.3 Simulation Procedure

Volume holographic gratings formed by spherical waves will be aperiodic within the volume hologram. However, if $d \ll r$, the aperiodic grating can be decomposed into locally planar sections [12,17] that vary in orientation across the hologram aperture as shown in Fig. 2, and r is the radius of curvature of a spherical wavefront. The localized approximation is valid since the recording and reconstruction waves are varying sufficiently slowly within each locally planar region. Therefore, in the locally planar section, the grating can be considered to be formed with two planar waves. The effects of all local planar regions are combined to determine the efficiency and image properties of the full hologram aperture.

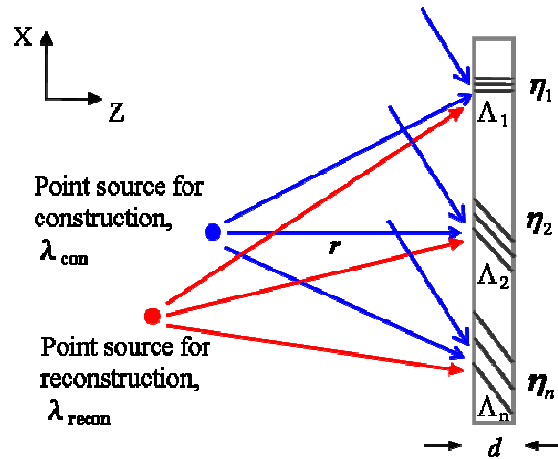


Fig. 2. Construction and reconstruction stages of an aperiodic grating.

Figure 3 shows a schematic diagram of the setup for making multiplexed aperiodic gratings. The gratings are multiplexed by moving the recording point source by Δz_{con} and adjusting the reference beam angle with $\Delta\theta$ for each exposure. In both RCW and ACW models, cross-coupling between gratings is minimal if the angular difference ($\Delta\theta$) between reference beams angles is greater than the angular selectivity of each grating. In addition, to simplify the calculation, the objective lens shown in Fig. 3 in the signal arm is assumed to be an aberration-free paraxial lens.

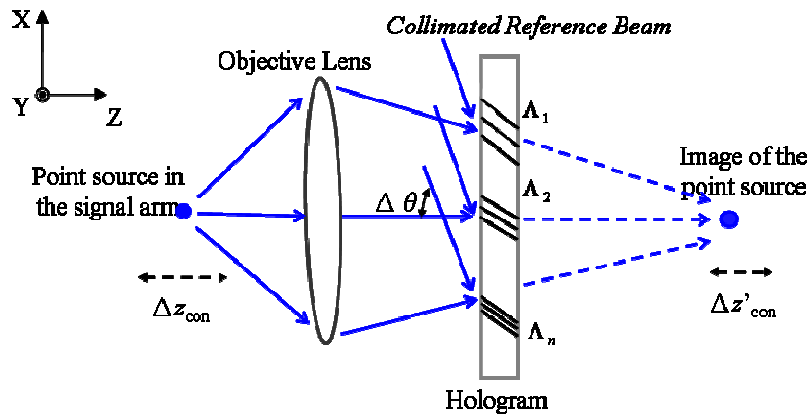


Fig. 3. Setup of multiplexed curved gratings.

To analyze multiplexed aperiodic gratings within a hologram, the procedure may be broken down into the following steps. 1) The image position of the point source is generated using either ray tracing function in Zemax or paraxial imaging equation, $\frac{1}{z'} = \frac{1}{z} + \frac{1}{f}$, where z and z' are distances of the Gaussian conjugate planes and f is the focal length of the objective lens. 2) The exposed area on the hologram is sampled with a large number N of sampling zones. The local grating periods and diffraction efficiencies are denoted as Λ_i and η_i , respectively, where $i = 1, \dots, N$. The spherical wave is decomposed into planar waves. In the individual sampling zone of the hologram, the grating is then considered to be formed by two planar waves, and the resulting grating vector is then computed. 3) The effects of thickness change, polarization state, and reconstruction wavelength on the properties of the grating are

considered, and the new grating vector is determined [8,9]. 4) RCW or ACW theory is used locally to determine the performance and calculate the diffraction efficiency (η_i) of the diffracted beam in each sampling zone. The total diffraction efficiency (η_{total}) across the hologram aperture from all sampling zones is obtained using Eq. (15). In the RCW model, the local diffraction efficiency is numerically computed as described in Section 2.1, and sequential ray tracing is performed to each sampling zone. In the ACW model the local diffraction efficiency is analytically computed using Eq. (12). Afterwards, non-sequential ray tracing is performed from each sampling zone to the imaging plane. Zemax[®] non-sequential ray tracing which incorporates the zero and first diffracted orders of each grating is implemented to estimate the crosstalk among gratings. To compare with RCW model and experimental results, the first order is more important and interesting since the first diffracted order dominates the volumetric diffraction effects in the VHIS. 5) This procedure is then repeated for each multiplexed grating by moving the constructed point source by Δz_{con} and changing the reference beam angle by $\Delta\theta$.

$$\eta_{total} = \left(\sum_i^N \eta_i \right) / N. \quad (15)$$

3. Measurements

3.1 Experimental Setup

Experimental samples of Phenanthrenquinone- (PQ-) doped Poly (methyl methacrylate) (PMMA) with thickness of ~1.5mm are used as the holographic recording materials. The holographic recording materials are formed using solutions of methylmethacrylate (MMA), 2,2 –Azobis(2-methylpropionitrile) (AIBN) and (phenanthrenquinone) (PQ) that are mixed in a respective weight ratio of 100:0.5:0.7 [16]. The mixed solution solidifies after curing at 50°C for 120hrs, completing the process. The PQ-doped PMMA holographic material can be formed with minimal shrinkage and refractive index change after processing, and provide high spectral and angular Bragg selectivity [16].

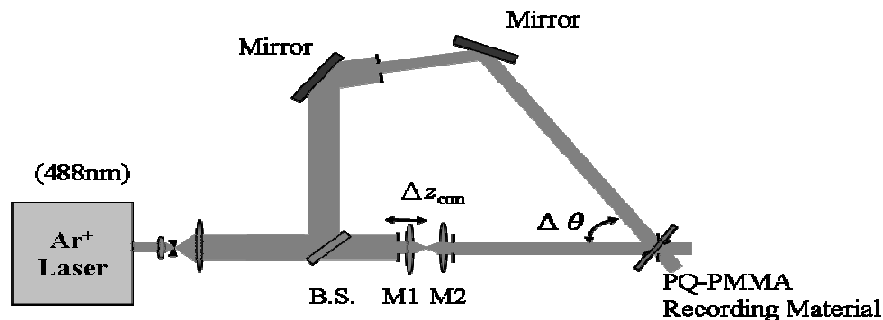


Fig. 4. Construction setup of the angle multiplexed holographic filters.

A multiplexed hologram is formed by superimposing interferometric exposures in the same volume of the recording material. In Fig. 4, multiplexed gratings are recorded with the set up using an Argon Ion Laser operating at the 488nm line. The reference beam is a planar wave and the point source recording positions in the signal arm are controlled by moving the first microscope objective lens (M1) with numerical aperture (NA) of 0.65 along the axial direction by Δz_{con} with each exposure. A second microscope objective lens (M2) with 0.55NA and 3.6mm focal length remains in a fixed position in the signal arm forming the point source. The nominal angle between the two arms is ~68° and is changed by $\Delta\theta = 1^\circ$ with each exposure to record a hologram with a different reference beam angle and point source location.

The angle settings, point source locations, and exposure time settings are automated using a LabView control system. The hologram exposures are varied to change the efficiency of the gratings within the hologram. Two multiplexed gratings were formed, and the chosen value of $\Delta\theta$ was to avoid crosstalk and image overlap during the reconstruction process [18].

3.2. Depth Separation and Selectivity Measurements

To quantitatively analyze the characteristics of aperiodic gratings multiplexed within a hologram, two different wavelengths of 488nm and 633nm were used for reconstruction in experiments to compare with the simulation results. A schematic diagram of the experimental VHIS setup is shown in Fig. 5. M3 is used to integrate the entire diffracted into the detector, and its focal length is 20mm.

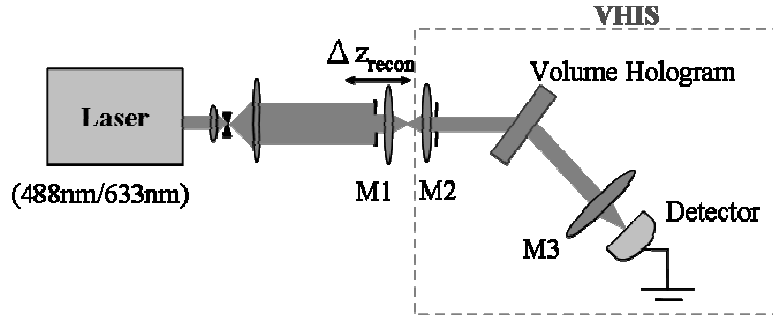


Fig. 5. Experimental setup for measuring depth selectivity, diffraction efficiency, and distance changes between the 488nm and 633nm lines.

The arrangement was used to characterize the VHIS with multiplexed gratings in depth selectivity, diffraction efficiency, and distance changes between different probing wavelengths. To observe the effect of changing the wavelength of the probing beam, we used TE-polarized light at 488nm (i.e., the same wavelength as recording) and 633nm. The longer wavelength is interesting because it provides deeper penetration depth in tissue objects. To measure the effects on depth separation and depth selectivity with different probe beams, the intensities of the diffracted beams, integrated across the image plane, were measured at a sequence of M1 locations separated by $1\mu\text{m}$. The diffraction efficiency was determined by using the relation:

$$\eta(\%) = \left(P_{diff} / P_{inc} \right) \times 100\%, \quad (12),$$

where P_{inc} is the power of the incident beam, and P_{diff} is the power of the diffracted beam.

Figure 6(a) shows experimental results of the point spread function in depth (PSF_z) at reconstruction wavelength of 488nm. Figure 6(b) shows experimental results of the PSF_z at the reconstruction wavelength of 633nm. Experimental results for the relationship between Δz_{con} and Δz_{recon} are plotted in Fig. 7. The slope of Δz_{con} and Δz_{recon} equals 1 when the recording and probing wavelengths are the same. However, when the probing wavelength changes, so does the slope [19]. This is verified in Fig. 7(b). The experimental data of peak diffraction efficiency (η) for the planar and curved gratings are annotated in the plots.

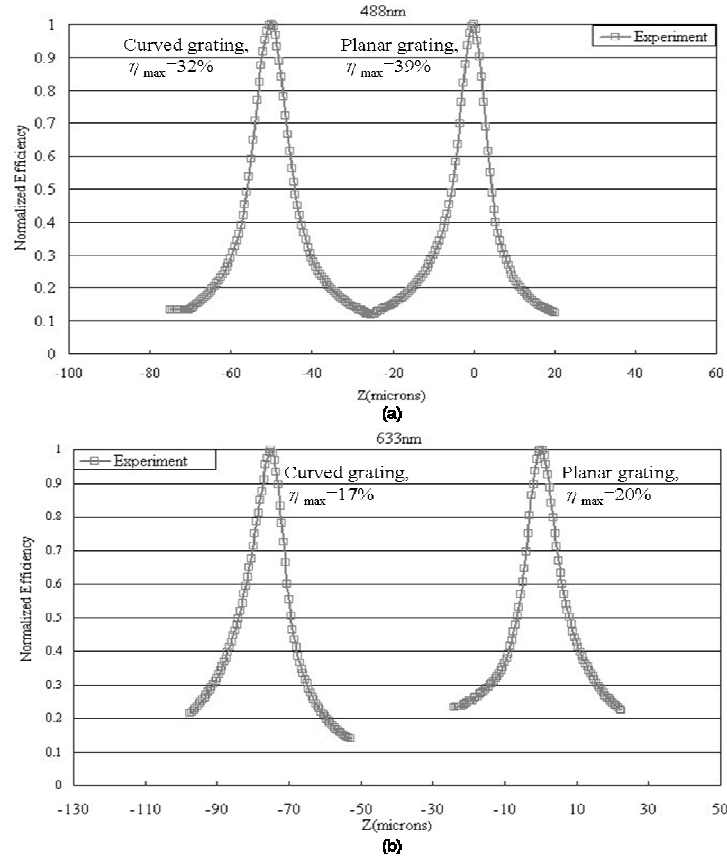


Fig. 6. (a) Experimental results of the depth selectivity for the hologram of two gratings at 488nm. η is normalized for easy comparison of the width of PSF_z , (b) Experimental results of the depth selectivity for the hologram of two gratings at 633nm. (Similarly normalized.)

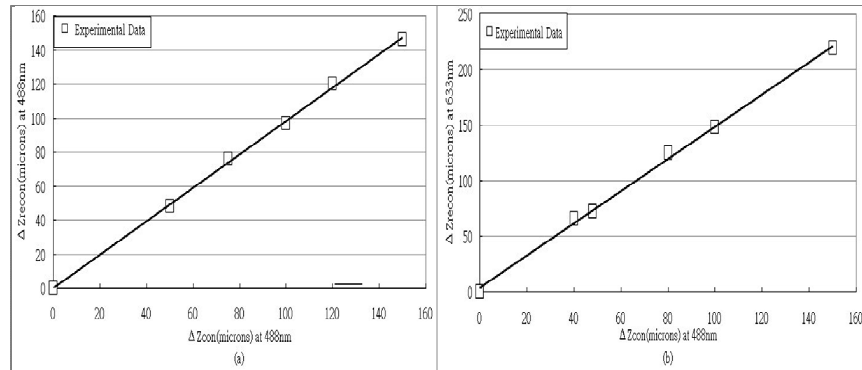


Fig. 7. Experimental results of the relationship between Δz_{con} and Δz_{rec} . (a) at the same wavelength of 488nm for both construction and reconstruction. (b) at the wavelength of 488nm for construction and 633nm for reconstruction.

4. Simulation Results

According to the method outlined in Subsection 2.3, a point source in the signal was set in the front focal point of the lens to form the first grating in the simulation. The second grating was formed by moving the point source away from the lens by $50\mu\text{m}$, $\Delta z_{con} = 50\mu\text{m}$. $N = 1000$

zones. Parameters in the simulation, i.e. hologram aperture and thickness, polarization, focal length, angle of probe beam, angle change, and longitudinal displacement between exposures, were chosen to be identical to the experimental values described in Section 3. Additional parameters were: absorption coefficient was 0.045(1/mm) at 488nm and 0.039(1/mm) at 633nm [20,21], the refractive index was 1.49, and the index modulation was 8×10^{-5} for the first grating and 7×10^{-5} for the second grating.

Figure 8(a) shows a VHIS setup generated by Zemax[®], and Fig. 8(b) shows the diffraction images on the detector plane of a point source with $\Delta z_{\text{recon}} = -2\mu\text{m}, -1\mu\text{m}, 0\mu\text{m}, 1\mu\text{m},$ and $2\mu\text{m}$. Figure 9(a) shows the ACW and RCW simulation modeling results of the point spread function in depth (PSF_z) at the reconstruction wavelength of 488nm, and the average full width of half maximum (FWHM) is $\sim 9\mu\text{m}$. Figure 9(b) shows the results of the PSF_z at the reconstruction wavelength of 633nm, and the average FWHM is $\sim 12\mu\text{m}$. The diffraction efficiency is also normalized for easy comparison of the width of PSF_z. The experimental data in Fig. 6 (a) and (b) have been duplicated in respective Fig. 9(a) and (b) to easily compare and validate modeling results with experimental results.

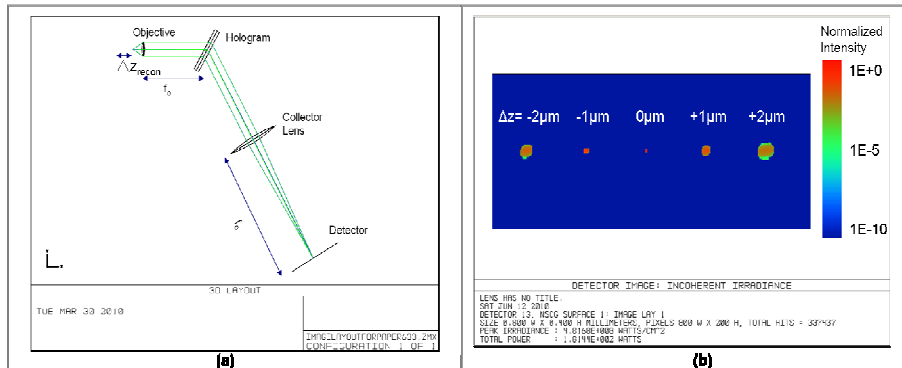


Fig. 8. (a) Layout of a VHIS produced by Zemax[®]. (b) Diffraction images (from the first diffracted order of a grating) in logarithm scale on the Zemax[®] detector plane using a point source with different Δz_{recon} .

In addition, Fig. 10(a) shows the simulation results for the relationship between Δz_{con} and Δz_{recon} using the same wavelength of 488nm. Figure 10(b) plots Δz_{con} vs Δz_{recon} when different wavelengths of 488nm and 633nm were used for recording and reconstruction, respectively.

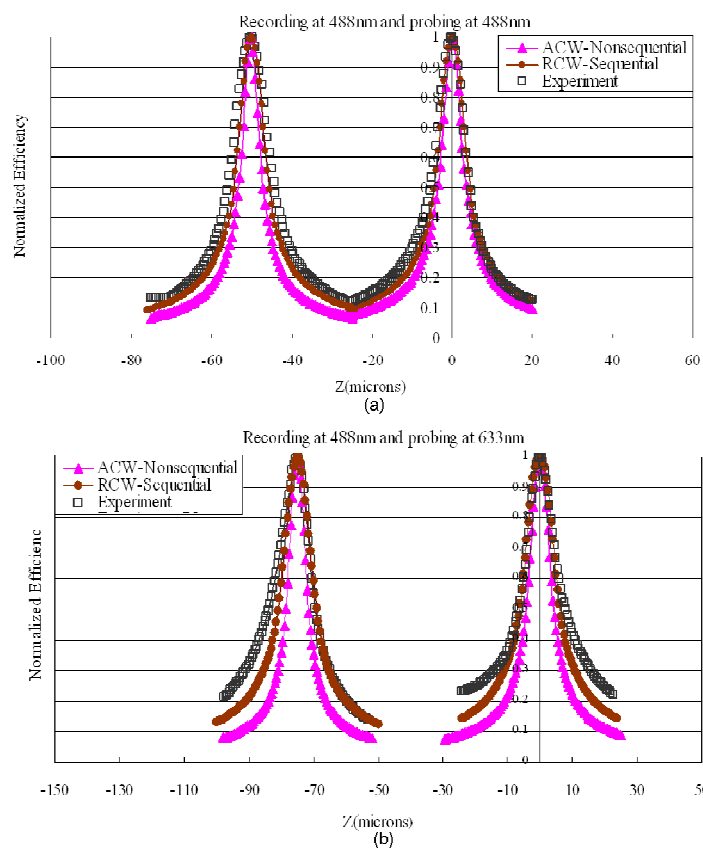


Fig. 9. (a) Experimental and numerical results of the depth selectivity at 488nm for the hologram of two gratings. (b) Experimental and numerical results of the depth selectivity at 633nm for the hologram of two gratings.

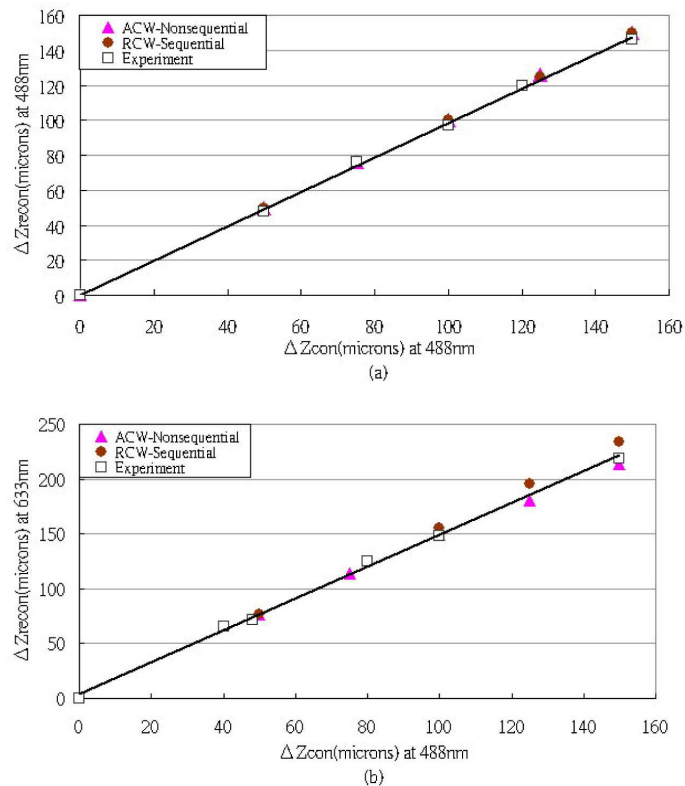


Fig. 10. (a) Experimental results and numerical analysis for the relationship between Δz_{con} and Δz_{recon} (a) at the same wavelength of 488nm. (b) at the wavelength of 488nm for construction and 633nm for reconstruction.

5. Conclusions

We described a new methodology based on the RCW and ACW in combination with ray tracing to accurately predict the effect of strong diffraction in image quality in a VHIS. Simulation results of curved holographic gratings in a VHIS based on our method that can be easily integrated into current commercial ray-tracing software such as Zemax[®] were confirmed with experiments and showed good agreement with the measurements.

Either aperiodic or periodic gratings in our experiments satisfy the condition of $d \ll r$, which indicates grating vectors are slowly varying along the lateral directions. Therefore, our approach utilizes localized approximation [11,12] and computes the local grating vector analytically in ACW or numerically in RCW. Thus, various types of volume holographic gratings may be simulated, including aperiodic and multiplexed gratings. By using two types of ray-tracing we can design VHIS in two ways: sequential ray-tracing for RCW and non-sequential for ACW. With sequential ray-tracing algorithms, a fast estimation for characterizing volume holographic gratings is obtained. If necessary, the non-sequential ray tracing algorithm can be easily extended to estimate crosstalk between multiplexed gratings with smaller reference beam angle separation.

Our findings indicate that the depth separation (*i.e.* Δz_{recon}) can be increased using longer wavelengths to probe multiplexed gratings, which are formed at shorter wavelengths. Therefore, the depth separation in the VHIS can be controlled by adjusting the operation wavelength of light sources. However, the diffraction efficiency of either aperiodic or periodic

gratings in the VHIS is lower using a longer probe wavelength of 633nm that is different with the construction wavelength of 488nm. In addition, the depth selectivity is degraded and the FWHM becomes wider when the longer wavelength of 633nm is used for reconstruction.

Our approach accurately predicts those experimental effects in the VHIS. Moreover, our approach can be used to simulate aberrations and optimize VHIS design to reduce aberrations using the optimization tools in Zemax[®]. Our model can be integrated with other ray-tracing software with proper modifications to theoretically predict the performance of multiplexed gratings in the VHIS. However, there is one limitation: localized grating approximation assumes that grating vectors are slowly varying along the lateral directions. Currently, we have verified the model for aperiodic and multiplexed imaging gratings formed in PQ-PMMA at 488nm and probed at 488nm/633nm. It is left for future research to extend the model for holograms recorded with aberrated or fast varying waves, investigation of optics with aberrations in VHIS to reach comparable depth selectivity with other imaging systems such as digital holographic microscopy [22], and optimization of system design using broadband illumination.

Acknowledgements

The authors gratefully acknowledge the support from the following sponsors: the National Institutes of Health (NIH-RO1CA134424) and the Singapore-MIT Alliance for Research and Technology Centre (SMART 015824-039). Authors Y. Luo and J. Castro contributed equally to this work.